Sensorless Control for Induction Machines Based on Square-Wave Voltage Injection

Young-Doo Yoon, *Member, IEEE*, and Seung-Ki Sul, *Fellow, IEEE*

***Abstract*—This paper presents a sensorless control for induction machines, using square-wave voltage injection. Multiple saliencies are considered, as well as saliency orientation shift according to loading conditions. These two nonideal phenomena severely degrade the performance of sensorless controls for induction machines. Multiple saliencies cause the position error signal to become distorted and make estimation of the rotor flux position difficult. Saliency orientation shift causes the estimated rotor flux position to drift from the actual rotor flux position, depending on the torque and speed. In this study, a sensorless algorithm based on square-wave voltage injection is adopted for induction machine control. When square-wave voltage is injected into the estimated synchronous reference frame, the harmonics of the error signal are lower than those of the conventional sinusoidal injection method. In addition, by injecting a square wave into the q-axis of the estimated synchronous reference frame instead of the d-axis, the saliency orientation shift is made smaller. Based on this study using square-wave voltage injection into the q-axis, the flux can be estimated with less error. Because of its enhanced rotor flux estimation performance, the proposed method provides better torque controllability than the conventional sinusoidal voltage injection method. Experimental results confirm the effectiveness of the proposed technique.**

***Index Terms*—Induction machine, multiple saliencies, saliency orientation shift, sensorless control, square-wave voltage injection.**

I. Introduction

INDUCTION machines are widely used in many industrial drive systems, due to attractive characteristics such as relatively low cost, reasonable size, robustness, and low maintenance. They are used not only for conventional drive applications, but also for high-performance applications [1], [2]. Most of these applications require adjustable-speed drives and/or suitable control performance, such as wide operational range and appropriate dynamics. Field-oriented control (FOC) has generally been adopted to obtain the required performance, which requires information on the rotor position [3]. Therefore, a mechanical shaft sensor (such as an encoder, resolver, and Hall sensor) is attached to the rotor shaft. However, these sensors increase the volume and cost of the drive system, and reduce the reliability.

In order to exploit the advantages (such as cost, size, and reliability) of these systems, a number of sensorless control techniques have been developed in recent years. As a result, the use of sensorless drives for ac motors is expanding in areas ranging from industrial applications to household electrical appliances [4]–[6]. Many sensorless techniques have been studied, and they can be classified into two categories: techniques based on back electromotive force (EMF) [7] and techniques based on saliency in the spatial impedance of the motor [8]–[20]. The former approach employs voltage models [7] and/or observers in the synchronous or stationary reference frame. It demonstrates reasonable performance in the medium- and high-speed regions, but cannot maintain its performance in the zero and/or low-speed region, where the back EMF drops significantly. The latter approach makes use of magnetic saliency. Spatial inductance variation is related to the rotor position; the rotor position can be identified by using this characteristic. Some algorithms inject test voltage signals over a sampling period to estimate the rotor position [8], [9]. However, such algorithms can be overly sensitive to parameter variation or measurement noise. This is because they detect inductance differences by using test voltage signals over a short time period. Moreover, they require additional hardware designed to measure phase currents at an arbitrary instant. But, it might be incompatible with industrial equipment.

High-frequency injection methods have also been proposed, typically involving injection of signals with frequencies ranging from several hundred hertz to several kilohertz. These also utilize the magnetic saliency. There are two approaches: rotating signal injection at the stationary reference frame [11], [12] and pulsating signal injection at the estimated synchronous reference frame [13]–[15]. These techniques can be applied to all kinds of ac machines, and they exhibit reasonable torque control capabilities at zero and/or low frequency, even under heavily loaded conditions. Square-wave voltage injection methods [16]–[18] have only recently been introduced. The square-wave injection scheme allows the bandwidths of position estimation and current regulation to be enhanced remarkably. Therefore, it provides better sensorless drive performance than the conventional sinusoidal voltage signal injection method.

Low-frequency injection methods [19], [20] have also been proposed. These are based on the excitation of small torques and rotor-speed oscillations, which induce oscillations in the

Manuscript received May 20, 2013; revised July 15, 2013 and July 29, 2013; accepted July 29, 2013. Date of current version February 18, 2014. This work was supported by the 2013 Research Fund of Myongji University and Human Resources Development Program (No. 20114010203030) of the Korea Institute of Energy Technology Evaluation and Planning (KETEP) grant funded by the Korea Government Ministry of Trade, Industry, and Energy. Recommended for publication by Associate Editor J. O. Ojo.

Y.-D. Yoon is with Myongji University, Yongin 449-728, Korea (e-mail: youngdoo.yoon@gmail.com).

S.-K. Sul is with the Seoul National University, Seoul 151-742, Korea (e-mail: sulsk@plaza.snu.ac.kr).

Color versions of one or more of the figures in this paper are available online at http://ieeexplore.ieee.org.

Digital Object Identifier 10.1109/TPEL.2013.2278103

0885-8993 © 2013 IEEE. Personal use is permitted, but republication/redistribution requires IEEE permission.
See http://www.ieee.org/publications_standards/publications/rights/index.html for more information.

back EMF. The oscillations can be detected in the stator voltage response at the injection frequency (typically in the 25–100 Hz range). These techniques also require additional devices designed to measure the stator voltages. When the devices are not available, the output of the current controller can be utilized. In this case, however, the nonlinear effects of the inverter must be overcome, such as dead-time effects and voltage drops of the power semiconductor switches.

Generally speaking, sensorless control of an induction machine via high-frequency signal injection exploits the impedance saliency of the machine due to magnetic saturation. However, multiple saliencies [21] and saliency orientation shift [22] occur with the injected signal. Multiple saliencies of an induction machine cause the position error signal to become distorted, and make accurate estimation of the rotor flux position difficult. Saliency orientation shift causes the estimated rotor flux position to deviate from the actual rotor flux position, depending on the operating conditions. Therefore, a compensation scheme is essential to maintain torque controllability.

In this paper, a sensorless control for induction machines is presented, using square-wave voltage injection into the q-axis of the estimated synchronous $d-q$ frame. When square-wave voltage is injected, the error signal has less harmonic noise compared to conventional sinusoidal signal injection. In addition, by injecting a square wave into the q-axis, the saliency orientation shift is smaller than when the signal is injected into the d-axis. As a consequence, the robustness and torque controllability of sensorless control of induction machines can be enhanced beyond what is obtained with the conventional sinusoidal voltage injection.

II. Sensorless Algorithm for Induction Machines Based on the Square-Wave Voltage Injection Method

Sensorless algorithms [11], [13] based on high-frequency injection methods exploit the impedance saliency of induction machines at the injected high frequency. Using this saliency, such sensorless algorithms can extract rotor flux information, even at zero stator frequency.

All signal injection methods for sensorless control of induction machines rely on the induced high-frequency current in the stationary reference framei^s_{dqsh}, which is the only measurable quantity. Hence, i^s_{dqsh} should be analyzed according to the voltage injection method. In [16], a technique employing square-wave voltage injection was adopted for sensorless control of induction machines. And, the high-frequency signal was analyzed under the assumption that the square-wave voltage is injected into the d-axis of the estimated synchronous reference frame. If the signal is injected into the q-axis, the signal can be analyzed in a similar way.

When square-wave voltage is injected into the d-axis of the estimated synchronous reference frame, the injected high-frequency voltage can be expressed as follows:

$$V^{\hat{e}}_{\mathrm{dsh}} = \begin{cases} V_{\mathrm{inj}}, & \text{half duty} \\ -V_{\mathrm{inj}}, & \text{otherwise} \end{cases}, \quad V^{\hat{e}}_{\mathrm{qsh}} = 0 \tag{1}$$

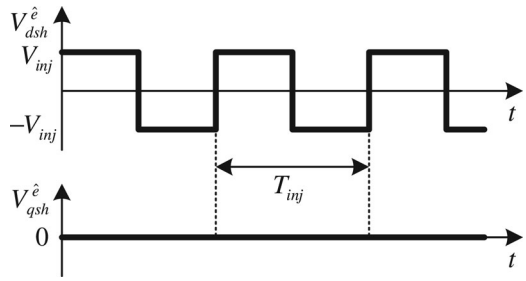

Fig. 1. Injection voltage waveform of the sensorless algorithm based on the square-wave injection method.

where $\hat{\theta}_e$ denotes the estimated rotor flux position and V_{inj} denotes the magnitude of the injected voltage. Fig. 1 shows an injected high-frequency voltage with period T_{inj}. The relationship between the injected high-frequency voltage and the induced current can be written as follows:

$$\begin{bmatrix} v^e_{\mathrm{dsh}} \\ v^e_{\mathrm{qsh}} \end{bmatrix} = [Z^e] \begin{bmatrix} i^e_{\mathrm{dsh}} \\ i^e_{\mathrm{qsh}} \end{bmatrix} = [Z^e]\,[R(\theta_e)] \begin{bmatrix} i^s_{\mathrm{dsh}} \\ i^s_{\mathrm{qsh}} \end{bmatrix} \tag{2}$$

where $[Z^e_h]$ denotes the high-frequency impedance matrix of induction machines in the synchronous reference frame. Therefore, the induced high-frequency current can be derived as follows:

$$\begin{aligned} \begin{bmatrix} i^s_{\mathrm{dsh}} \\ i^s_{\mathrm{qsh}} \end{bmatrix} &= [R(\theta_e)]^{-1}\,[Z^e]^{-1} \begin{bmatrix} v^e_{\mathrm{dsh}} \\ v^e_{\mathrm{qsh}} \end{bmatrix} \\ &= [R(\theta_e)]^{-1}\,[Z^e]^{-1} \left[R(\tilde{\theta}_e)\right] \begin{bmatrix} v^{\hat{e}}_{\mathrm{dsh}} \\ v^{\hat{e}}_{\mathrm{qsh}} \end{bmatrix}. \end{aligned} \tag{3}$$

Under the assumption that the high-frequency signal is injected and the injected frequency ω_h is at least one order of magnitude larger than the fundamental frequency ω_e, the voltage drops of the stator resistances R^e_{dh} and R^e_{qh} are generally much smaller than those of high-frequency inductances L^e_{dh} and L^e_{qh}. And, the cross-coupling voltages $-\omega_e L^e_{\mathrm{dh}} i^e_{\mathrm{qsh}}$ and $\omega_e L^e_{\mathrm{qh}} i^e_{\mathrm{dsh}}$ are also much smaller than the voltage drops of the high-frequency inductances. Thus, the high-frequency impedance $[Z^e_h]$ can be simplified as follows:

$$\begin{aligned} \begin{bmatrix} v^e_{\mathrm{dsh}} \\ v^e_{\mathrm{qsh}} \end{bmatrix} = [Z^e] \begin{bmatrix} i^e_{\mathrm{dsh}} \\ i^e_{\mathrm{qsh}} \end{bmatrix} &= \begin{bmatrix} R^e_{\mathrm{dh}} + L^e_{\mathrm{dh}} \dfrac{d}{dt} & -\omega_e L^e_{\mathrm{qh}} \\ \omega_e L^e_{\mathrm{dh}} & R^e_{\mathrm{qh}} + L^e_{\mathrm{qh}} \dfrac{d}{dt} \end{bmatrix} \\ &\times \begin{bmatrix} i^e_{\mathrm{dsh}} \\ i^e_{\mathrm{qsh}} \end{bmatrix} \approx \begin{bmatrix} L^e_{\mathrm{dh}} & 0 \\ 0 & L^e_{\mathrm{qh}} \end{bmatrix} \frac{d}{dt} \begin{bmatrix} i^e_{\mathrm{dsh}} \\ i^e_{\mathrm{qsh}} \end{bmatrix}. \end{aligned} \tag{4}$$

When the square-wave voltage of (1) is injected, the corresponding $\Delta i^s_{\mathrm{dqsh}}$ can be expressed as (5) under the assumption that (6) holds. Here, "Δ" represents the difference between the present and previous sampling instant values

$$\begin{aligned} \begin{bmatrix} \Delta i^e_{\mathrm{dsh}} \\ \Delta i^e_{\mathrm{qsh}} \end{bmatrix} &\approx \begin{bmatrix} \cos(\theta_e) & -\sin(\theta_e) \\ \sin(\theta_e) & \cos(\theta_e) \end{bmatrix} \begin{bmatrix} \cos(\tilde{\theta}_e) V^{\hat{e}}_{\mathrm{dsh}} \Delta T / L^e_{\mathrm{dh}} \\ -\sin(\tilde{\theta}_e) V^{\hat{e}}_{\mathrm{dsh}} \Delta T / L^e_{\mathrm{qh}} \end{bmatrix} \\ &= V^{\hat{e}}_{\mathrm{dsh}} \Delta T \begin{bmatrix} \cos(\theta_e)\cos(\tilde{\theta}_e)/L^e_{\mathrm{dh}} + \sin(\theta_e)\sin(\tilde{\theta}_e)/L^e_{\mathrm{qh}} \\ \sin(\theta_e)\cos(\tilde{\theta}_e)/L^e_{\mathrm{dh}} - \cos(\theta_e)\sin(\tilde{\theta}_e)/L^e_{\mathrm{qh}} \end{bmatrix} \end{aligned} \tag{5}$$

$$\begin{bmatrix} i^e_{\mathrm{dsh}} \\ i^e_{\mathrm{qsh}} \end{bmatrix} \approx \int \begin{bmatrix} L^e_{\mathrm{dh}} & 0 \\ 0 & L^e_{\mathrm{qh}} \end{bmatrix}^{-1} \begin{bmatrix} v^e_{\mathrm{dsh}} \\ v^e_{\mathrm{qsh}} \end{bmatrix} dt \tag{6}$$

where ΔT denotes the sampling period. To include the polarity of the injected voltage, (5) can be modified as follows:

$$\Delta i^{s\prime}_{\mathrm{dsh}} = \begin{cases} \Delta i^s_{\mathrm{dsh}}, & \text{if } V^{\hat{e}}_{\mathrm{dsh}} > 0 \\ -\Delta i^s_{\mathrm{dsh}}, & \text{otherwise} \end{cases}$$

$$\Delta i^{s\prime}_{\mathrm{qsh}} = \begin{cases} \Delta i^s_{\mathrm{qsh}}, & \text{if } V^{\hat{e}}_{\mathrm{dsh}} > 0 \\ -\Delta i^s_{\mathrm{qsh}}, & \text{otherwise.} \end{cases} \tag{7}$$

Finally, the signal denoted by $\Delta i^{s\prime}_{\mathrm{dqsh}}$ can be expressed as

$$\begin{bmatrix} \Delta i^{s\prime}_{\mathrm{dsh}} \\ \Delta i^{s\prime}_{\mathrm{qsh}} \end{bmatrix} = V_{\mathrm{inj}} \Delta T \cdot \begin{bmatrix} \dfrac{\cos(\theta_e)\cos(\tilde{\theta}_e)}{L^e_{\mathrm{dh}}} + \dfrac{\sin(\theta_e)\sin(\tilde{\theta}_e)}{L^e_{\mathrm{qh}}} \\ \dfrac{\sin(\theta_e)\cos(\tilde{\theta}_e)}{L^e_{\mathrm{dh}}} - \dfrac{\cos(\theta_e)\sin(\tilde{\theta}_e)}{L^e_{\mathrm{qh}}} \end{bmatrix}. \tag{8}$$

In order to intuitively understand the dependency of the high-frequency current on the rotor flux position, (8) can be simplified to (9) under the assumption that the estimation error of the rotor flux position ($\tilde{\theta}_e = \theta_e - \hat{\theta}_e$) is sufficiently small

$$\begin{bmatrix} \Delta i^{s\prime}_{\mathrm{dsh}} \\ \Delta i^{s\prime}_{\mathrm{qsh}} \end{bmatrix} \approx V_{\mathrm{inj}} \Delta T \cdot \begin{bmatrix} \dfrac{\cos(\theta_e)}{L^e_{\mathrm{dh}}} \\ \dfrac{\sin(\theta_e)}{L^e_{\mathrm{dh}}} \end{bmatrix} \text{(Under assumption that } \tilde{\theta}_e \approx 0\text{)}. \tag{9}$$

As (9) implies, $\Delta i^{s\prime}_{\mathrm{dqsh}}$ provides direct access to the rotor flux position θ_e. $\Delta i^{s\prime}_{\mathrm{dsh}}$ and $\Delta i^{s\prime}_{\mathrm{qsh}}$ are expressed in terms of the cosine and sine, respectively, of the rotor flux position. Therefore, using the arctangent function, the rotor flux position, $\theta_{e\mathrm{Cal}}$ can be obtained from $\Delta i^{s\prime}_{\mathrm{dqsh}}$ via (10). Moreover, the error signal of the position estimator $f(\tilde{\theta}_e)$ can be obtained from $\theta_{e\mathrm{Cal}}$ via (11). Using an observer or a state filter, $\hat{\theta}_e$ and $\hat{\omega}_e$ can then be estimated:

$$\theta_{e\mathrm{Cal}} = \mathrm{atan2}\left(\Delta i^{s\prime}_{\mathrm{qsh}},\ \Delta i^{s\prime}_{\mathrm{dsh}}\right) \tag{10}$$

$$f(\tilde{\theta}_e) \equiv \theta_{e\mathrm{Cal}} - \hat{\theta}_e = K_{\mathrm{error},d}\tilde{\theta}_e \tag{11}$$

$$K_{\mathrm{error},d} = \frac{L^e_{\mathrm{qh}} - L^e_{\mathrm{dh}}}{L^e_{\mathrm{qh}}} \tag{12}$$

where $K_{\mathrm{error},d}$ denotes the relationship between the estimation error $\tilde{\theta}_e$ and the error signal $f(\tilde{\theta}_e)$ when the signal is injected into the d-axis.

Using (10) and (11), $\theta_{e\mathrm{Cal}}$ and $f(\tilde{\theta}_e)$ can be obtained at every sampling instant, with no LPF. This means that the error signal could be obtained without time delay, which is crucial for extending the bandwidth of a sensorless control. Hence, position estimation performance can be enhanced remarkably.

Equations (9)–(11) are derived under the assumption that the position estimation error is nearly zero. When the error becomes large, the error signal $f(\tilde{\theta}_e)$ is not proportional to the error. In order to investigate the acceptable estimation error range, the error signal was simulated with the parameters of the tested machine. Fig. 2 shows the relationship between the position estimation error and the normalized error signal by $K_{\mathrm{error},d}$. When the estimation error is less than 0.5 rad, the normalized error signal is identical to the estimation error. Within this estimation error range, the position observer can estimate the position, and the speed and current control loops work well.

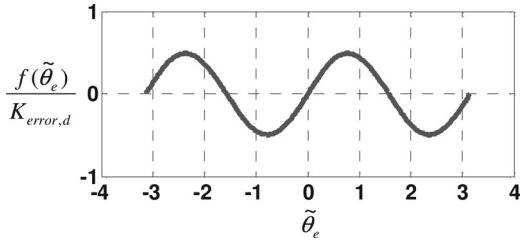

Fig. 2. Relationship between the position estimation error and the normalized error signal by $K_{\mathrm{error},d}$.

However, when the estimation error becomes larger than 0.5 rad. due to the rapid and heavy load variation, the normalized error signal is not identical to the position error. In that case, the performance of the position observer would be degraded. As a result, the performance of the speed and current control would be also degraded.

If the high-frequency impedance does not have a saliency, the $\Delta i^{s\prime}_{\mathrm{dqsh}}$ representation of the estimated rotor flux position $\hat{\theta}_e$ is given by (13), which is simply the voltage signal injection position and does not represent the actual rotor flux position. Therefore, this method cannot be applied when a saliency does not appear, or disappears under specified operating conditions.

If the saliency of the high-frequency impedance does not exist, $\Delta i^{s\prime}_{\mathrm{dqsh}}$ represents the estimated rotor flux position, $\hat{\theta}_e$ as (13), which is only the voltage signal injection position. It does not represent the real rotor flux position. Therefore, the method cannot be applied when the saliency does not appear or disappears under any certain operating conditions.

$$\begin{aligned} \begin{bmatrix} \Delta i^{s\prime}_{\mathrm{dsh}} \\ \Delta i^{s\prime}_{\mathrm{qsh}} \end{bmatrix} &= V_{\mathrm{inj}} \Delta T \cdot \begin{bmatrix} \dfrac{\cos(\theta_e)\cos(\tilde{\theta}_e)}{L^e_h} + \dfrac{\sin(\theta_e)\sin(\tilde{\theta}_e)}{L^e_h} \\ \dfrac{\sin(\theta_e)\cos(\tilde{\theta}_e)}{L^e_h} - \dfrac{\cos(\theta_e)\sin(\tilde{\theta}_e)}{L^e_h} \end{bmatrix} \\ &= \frac{V_{\mathrm{inj}}\Delta T}{L^e_h} \cdot \begin{bmatrix} \cos(\hat{\theta}_e) \\ \sin(\hat{\theta}_e) \end{bmatrix}. \end{aligned} \tag{13}$$

An overall block diagram of a sensorless algorithm based on the square-wave voltage injection method is shown in Fig. 3. The demodulation process simply consists of (7), (10), and the Δ function. Moreover, because the injection voltage is a square wave, the injection frequency can be increased up to the switching frequency [18], making it possible to clearly distinguish the injection frequency from the fundamental frequency of the motor. Accordingly, interference between the injection voltage and the output voltage of the current controller could be greatly reduced. Thanks to this reduced interference, the control bandwidths of the current regulator and speed regulator could be

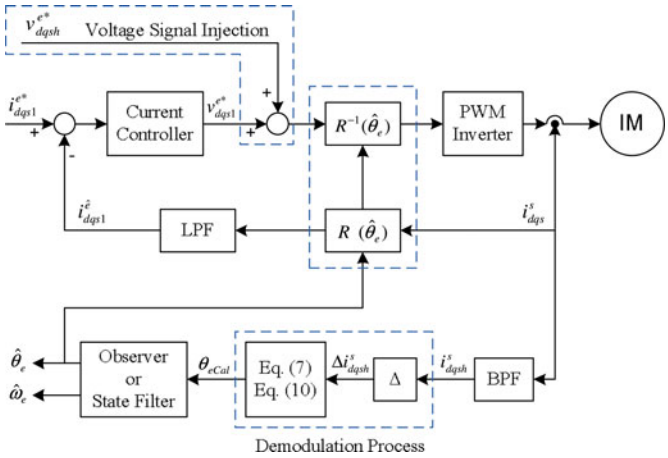

Fig. 3. Block diagram of the sensorless algorithm based on square-wave voltage injection method.

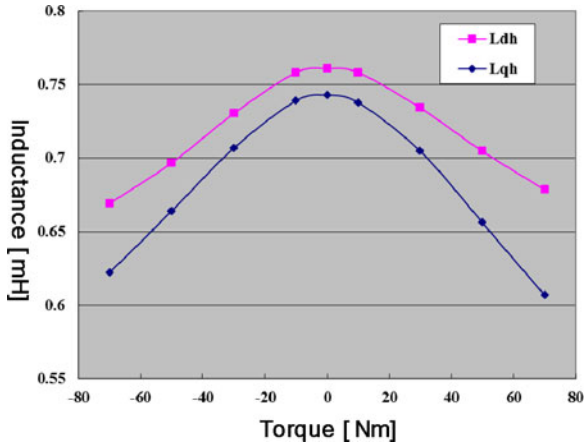

Fig. 4. High-frequency impedance of the tested induction machine according to the load torques.

TABLE I
NOMINAL PARAMETERS OF THE TESTED MOTOR

Quantity	Value [Unit]
Rated Power	11 [kW]
Rated Speed	1750 [r/min]
Rated Torque	60 [Nm]
Rated Line Frequency	59.6 [Hz]
Number of Pole	4
Rated Line Voltage	180 [V_{RMS}]
Rated Current	45 [A_{RMS}]
Overall Inertia	0.098 [kg·m^2]

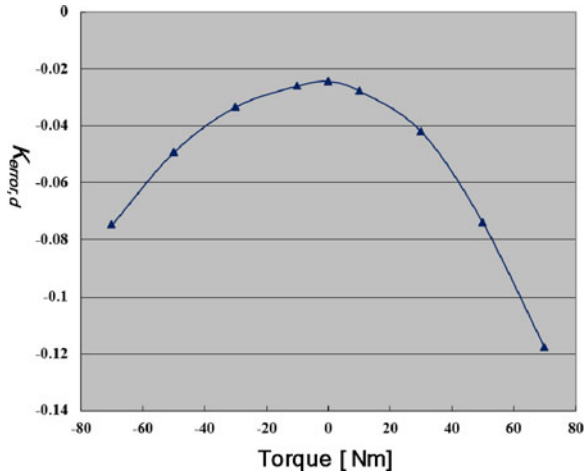

Fig. 5. $K_{\mathrm{error},d}$ according to load torques.

expanded. As a result, the dynamic performance of the sensorless drive system could be enhanced [16]–[18].

General-purpose induction machines have symmetric mechanical shapes, and hence, do not have saliencies. In this case, a sensorless algorithm based on saliency would not be applicable. However, by injecting a high-frequency signal, an induction machine could be given a saliency at the injection frequency, and sensorless techniques could then be utilized [11], [13].

Unfortunately, sensorless drives for induction machines cannot take full advantage of the high-frequency signal injection scheme, for the following reasons. In the first place, the injection frequency for induction machines is limited up to a range of about 1 kHz. Beyond this range, the high-frequency saliency of the machine may decrease, so that estimation of the rotor flux position may become unstable and the sensorless drive may fail. In order to obtain a stable saliency, the injection signal must generate enough flux to saturate the machine. When the magnitude of the injection voltage is maintained and the injection frequency increases, the magnitude of the generated flux from the injected signal decreases and the sensorless drive may fail. In order for the injection signal to generate sufficient flux, the magnitude of the injection voltage must increase according to the injection frequency. However, due to the fixed dc-link voltage, the available injection voltage is also limited. In this study, the frequency and magnitude of the injection voltage are set at 800 Hz and 125 V, respectively, in order to generate sufficient flux.

Fig. 4 shows the high-frequency impedance of the tested machine according to the load torques. The nominal parameters of the machine are listed in Table I. Fig. 5 shows $K_{\mathrm{error},d}$ according to the load torques. When the signal is injected into the d-axis, $K_{\mathrm{error},d}$ has a negative value. Other issues pertaining to d-axis signal injection are described in the next chapter.

III. The Proposed Sensorless Algorithm for Induction Machines

An injected high-frequency signal introduces high-frequency flux linkage through the leakage flux paths, and these leakage paths become saturated with both the high-frequency flux and the main flux. Machines typically have a number of localized leakage flux paths, and these also become saturated [23]. Due to these localized saturations, multiple saliencies and saliency orientation shift (SOS) occur. These phenomena have a more serious impact on induction machines than on other ac machines with inherent magnetic saliency of the rotor, the difference being that the saliency of an induction machine results from the saturation introduced by strong injection signals. These two

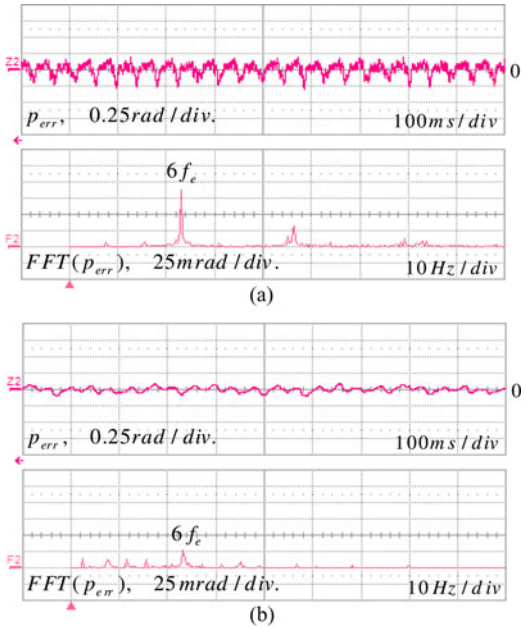

Fig. 6. Position estimation error signals and their FFT results at 50% of the rated torque: (a) with the conventional synchronous pulsating signal injection method and (b) with the square-wave signal injection method.

phenomena should be carefully considered to enhance the performance of sensorless control of induction machines.

Localized saturations can cause multiple saliencies to occur, in which case, the estimated position of the rotor flux might be the locally saturated position of the leakage flux paths, rather than the actual position of the rotor flux. In order to clearly demonstrate the multiple-saliency phenomenon, the position estimation error was experimentally measured by running the induction machine under sensored indirect rotor flux orientation (IRFO) control [22]. Fig. 6 shows the position error $\tilde{\theta}_e = \theta_e - \hat{\theta}_e$, and their FFT results at 50% of the rated torque and an operating speed of 100 r/min.

From Fig. 6(a) and (b), there are position estimation errors with both the conventional pulsating sinusoidal signal injection method and the square-wave signal injection method. Although the injection methods and the corresponding demodulation processes are different, the other operating conditions are the same. Due to the multiple saliencies, the error signal exhibits $6f_e$ harmonics after the demodulation process [22]. The harmonics must be separated from the position error signal in the estimator to obtain the correct rotor flux position. The separation could be implemented on the basis of a rigorous commissioning process or a sophisticated filtering process. However, this is quite difficult to accomplish, and its performance is unsatisfactory in most of the high-torque operating region. In addition to the multiple-saliency phenomenon, nonlinear effects of the inverters (such as dead-time and zero-current clamping effects) are also a possible source of the $6f_e$ harmonics of the error signal. Due to these harmonics, the bandwidth of the position estimator shrinks and the dynamics of the estimator are too sluggish.

As shown in Fig. 6, the error signal of the square-wave injection method exhibits less sixth harmonics of position estimation error compared with sinusoidal signal injection. This difference might come from the difference of the demodulation processes of two methods. After the demodulation process of sinusoidal-wave injection method, the position estimation error shows the error signal at the injection frequency. In this process, the error signal has not only the real position error signal but also the harmonics that are generated by the multiple saliencies. So, the position estimation error shows several harmonics. On the other hand, the demodulation process of square-wave injection method utilizes the difference of high-frequency current between the present and previous sampling instant values. And, in order to get the real position error selectively rather than other harmonics, the sampling frequency is set as four times of the injection frequency. Due to this process, the error signal reveals smaller magnitude of harmonics.

Comparisons of Fig. 6(a) and (b) show that the harmonics generated by square-wave injection are much smaller than those generated by sinusoidal-wave injection. Thus, by using the square-wave signal injection method and its corresponding demodulation process, the effect of the multiple-saliency phenomenon can be reduced, and the error signal might be made robust against multiple saliencies. As a result, the multiple-saliency problem could be overcome by utilizing the square-wave signal injection method.

In addition to the multiple-saliency phenomenon, SOS is also an issue. SOS appears particularly distinct in the case of nonsalient-pole machines such as induction machines and surface mounted permanent magnet machines. It can be explained that the stator current causes changes of the local saturation level. Loading of the machine increases the main and leakage flux levels and displaces the most saturated regions [22], [24]. The position of the high-frequency saliency shifts from the actual rotor flux position, depending on the load conditions.

This causes a position estimation error, and severely degrades the performance of sensorless control under high-torque operation. The estimated position from the error signal should be compensated according to the load conditions. The compensation angle for SOS can be identified via an offline test of the induction machine, in which the machine is operated under sensored IRFO control. The estimated rotor flux position obtained by the square-wave signal injection method is monitored and compared to the sensored IRFO angle. Fig. 7 shows the compensation angle $\phi = \theta_{e,\mathrm{IRFO}} - \hat{\theta}_{e,SAT}$ when the square-wave signal is injected into the d-axis and the q-axis, respectively. It is almost linear. As the figure indicates, q-axis injection yields a much smaller angle than d-axis injection. Although Fig. 7 shows the compensation angle for square-wave signal injection, similar phenomena occur in sinusoidal signal injection, as well as in other injection schemes.

SOS depends not only on load conditions, but also on operating speeds. Fig. 8 shows the SOS according to speed. As the figure indicates, SOS variation is less dependent on speed with q-axis injection than with d-axis injection. The influence by operating speed is as large as that by loading condition. However, the influence is not a linear function of operating speed, but it is a linear function with a discontinuous point where the polarity of operating speed changes. This compensation might

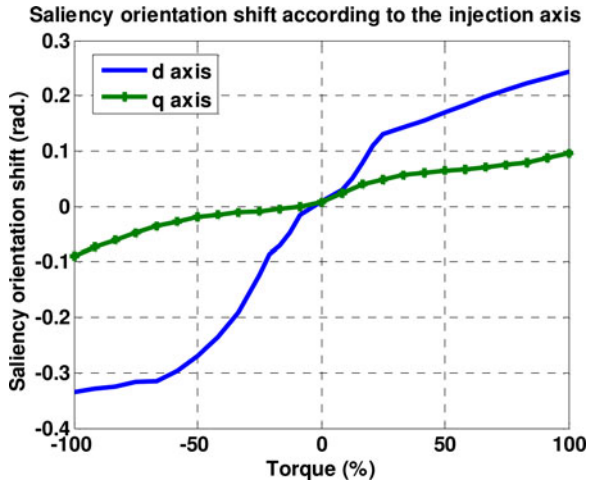

Fig. 7. Compensation angle according to the injection axis and the torque.

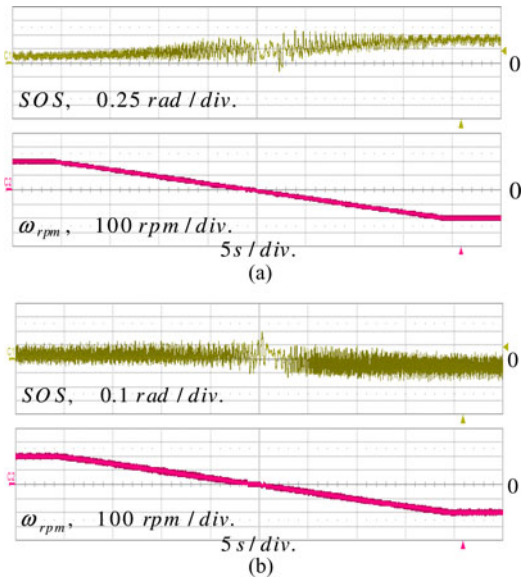

Fig. 8. Compensation angle according to the rotational speed at 50% of the rated torque: (a) with d-axis injection and (b) with q-axis injection.

cause some discontinuity on the sensorless control. Fortunately, the maximum SOS by speed is less than 3 degree in electrical angle, so that SOS by speed might be negligible.

Based on these results, it can be concluded that by injecting a square-wave signal into the q-axis, the compensation angle for SOS can be kept small in the context of the overall operating conditions, and estimation of the angle is robust with respect to torque and speed variations. The rotor flux angle for the field-oriented control can be expressed as

$$\hat{\theta}_e = \hat{\theta}_{e,\mathrm{SAT}} + \phi(T_e) \tag{14}$$

where $\hat{\theta}_{e,SAT}$ denotes the estimated position of the rotor flux linkage from square-wave signal injection, and $\phi\,(T_e)$ denotes the SOS compensation angle. In this case, the compensation angle could easily be obtained from a simple one-dimensional lookup table or a simplified linear function. In experiments, it is implemented as a linear function of the torque command.

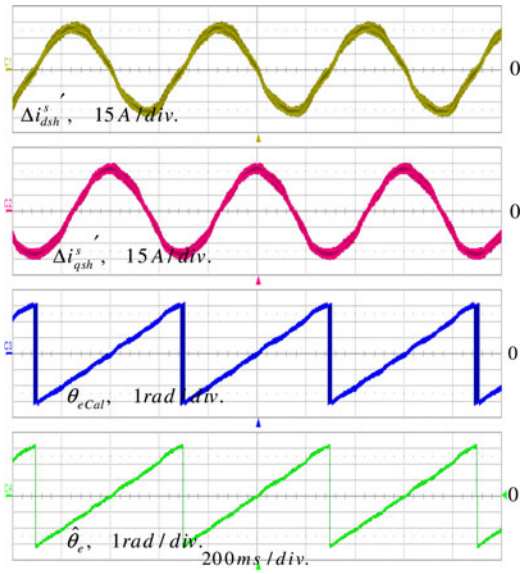

Fig. 9. Rotor flux position estimation performance.

This study has discovered the merits of q-axis injection for induction machines. In the case of the other machines such as surface-mounted permanent magnet machines (SPMs) and interior-mounted permanent magnet machines (IPMs), more researches need to confirm the merits of q-axis injection. These are still in progress.

IV. Experimental Results

Experiments with a general-purpose induction machine were performed to verify the effectiveness of the proposed method. The induction machine was an 11-kW four-pole closed-slot skewed-rotor machine; its nominal parameters are listed as Table I. It was coupled to a permanent magnet synchronous servo motor, which served as a load machine. Square-wave voltage was injected into the q-axis of the estimated synchronous reference frame to reduce the effects of multiple saliencies and saliency orientation shift. The magnitude of the injection voltage was 125 V and the frequency was 800 Hz. The induction machine was driven by the proposed sensorless speed control, and the load machine was driven by torque control.

Fig. 9 shows the rotor flux position estimation performance of the proposed sensorless control under constant-speed operation at 50 r/min. The signals$\Delta i^{s\prime}_{\mathrm{dqsh}}$, $\theta_{e\mathrm{Cal}}$, and $\hat{\theta}_e$ are plotted together. In (9), $\Delta i^{s\prime}_{\mathrm{dsh}}$ and $\Delta i^{s\prime}_{\mathrm{qsh}}$ are expressed in terms of the cosine and sine, respectively, of the rotor flux position. In Fig. 9, however, $\Delta i^{s\prime}_{\mathrm{dsh}}$ and $\Delta i^{s\prime}_{\mathrm{qsh}}$ have the respective forms of $-\sin\hat{\theta}_e$ and $\cos\hat{\theta}_e$. This is because the voltage signal was injected into the q-axis of the estimated synchronous reference frame, whereas (9) was derived under the assumption that the voltage signal is injected into the d-axis. When the signal is injected into the q-axis, $\theta_{e\mathrm{Cal}}$ and $K_{\mathrm{error},d}$ are modified as follows:

$$\theta_{e\mathrm{Cal}} = a\tan2\left(-\Delta i^{s\prime}_{\mathrm{dsh}},\ \Delta i^{s\prime}_{\mathrm{qsh}}\right) \tag{15}$$

$$K_{\mathrm{error},q} = \frac{L^e_{\mathrm{dh}} - L^e_{\mathrm{qh}}}{L^e_{\mathrm{dh}}}. \tag{16}$$

Using the arctangent function and $\Delta i^{s\prime}_{\mathrm{dqsh}}, \theta_{e\mathrm{Cal}}$ was calculated. $\hat{\theta}_e$ was estimated via a state filter. As Fig. 9 indicates, the rotor flux position was closely estimated.

Sensorless algorithms based on injection methods are utilized when the operating speed is low. Over 100 r/min in the case of four-pole machines with 60 Hz rated frequency, induction machines can be driven by adaptive speed observer algorithms [25] instead of sensorless algorithms based on injection methods. Hence, over that speed, the high-frequency voltage would not be injected.

Under that speed, high-frequency voltage is injected and the magnitudes of the injected voltage and the induced current are quite large. So, the voltage and current for induction machine drives might be insufficient. However, since the operating speed is low, the voltage is also small. At the operating speed of 200 r/min, the required voltage for the induction machine drives at rated torque condition is less than 30 V based on the calculation with the tested machine parameters. On the other hand, due to the large amount of high-frequency voltage injection, the induced current is also quite large as 37 A. However, because the frequency range of the induced current is different from the fundamental one, the maximum torque current can be calculated as (17). Considering the rated current of the machine, around 80% of the rated torque can be produced when the high-frequency voltage is injected.

$$i^e_{qs_\max} = \sqrt{(I_{\max})^2 - (I^e_{ds})^2 - (I_{\mathrm{inj}})^2} \tag{17}$$

where $I_{\max}$ means the rated current of induction machine and, I^e_{ds} means the magnitude of the flux current and, I_{inj} means the magnitude of the induced high-frequency current.

Generally, sensorless algorithms using injection methods make some acoustic noises. The proposed method also makes acoustic noise. And, this sensorless algorithm is proposed for general-purpose induction machines that do not have any additional modifications on the rotor. In this case, sensorless algorithms estimate the rotor flux position instead of the rotor position, and the rotor position cannot be estimated. In order to evaluate the control performance, the comparison between the estimated speed and real speed from encoder were demonstrated in Figs. 10–13 instead of the comparison between the estimated position and real position.

Fig. 10 shows the performance of the sensorless speed control under slow reference speed variation near zero speed at the rated torque. The reference speed was changed from 100 to –100 r/min, and vice versa, at the slow rate of 10 (r/min)/s. $\hat{\theta}_e$ had some distortions due to the multiple saliencies. These distortions produced a ripple in $\hat{\omega}_{\mathrm{rpm}}$, resulting in a ripple in the torque of the tested motor, denoted by T_e_IM.

Due to the q-axis injection, some torque ripple might appear in the machine. However, the frequency of the torque ripple is the injection frequency so that mechanical damping of the test system significantly attenuated the torque ripple. A conspicuous vibration on rotor shaft did not appear and the torque ripple does not corrupt the drive system in the experiments. But, in small drive systems that have relatively small inertia and mechanical damping, the proposed method might make the rotor shaft vibrate due to the torque ripples.

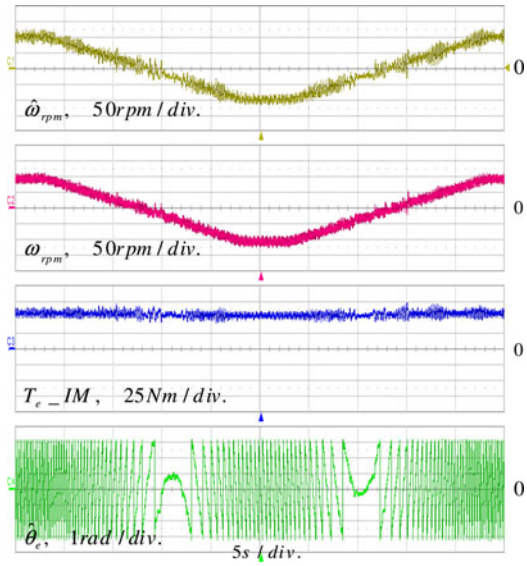

Fig. 10. Slow speed reversal at the rated torque.

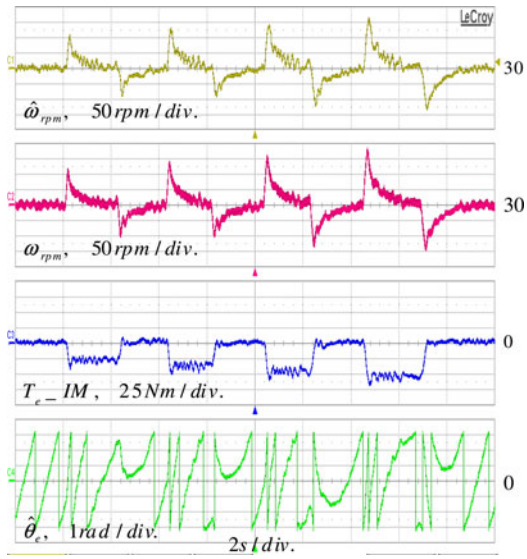

Fig. 11. Experimental results under load variation at a constant speed of 30 r/min.

Fig. 11 shows the waveforms under load variation. The load torque was applied in steps, from 0% to 50%, from 0% to 67%, from 0% to 83%, and from 0% to 100% of the rated torque, at a constant speed of 30 r/min. Fig. 12 shows the waveforms obtained with the same load variation at zero speed.

Fig. 13 shows the waveforms obtained when the synchronous frequency was null. A load torque of 44 N·m was applied at a constant speed of –20 r/min. Because of the negative rotational speed and positive slip speed for the positive torque, the angular speed of the rotor flux was null for 10 seconds. In spite of

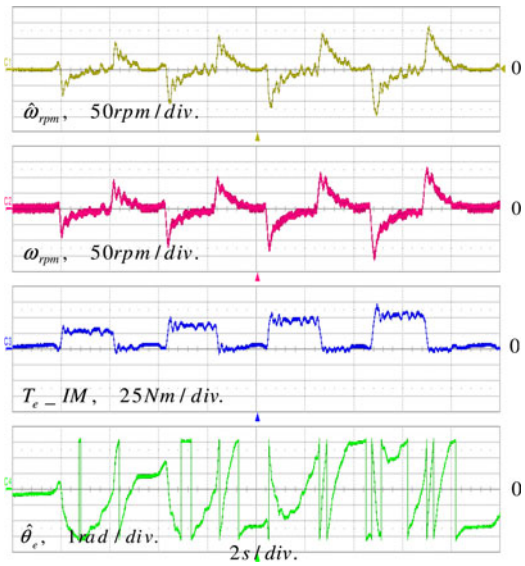

Fig. 12. Experimental results under load variation at zero speed.

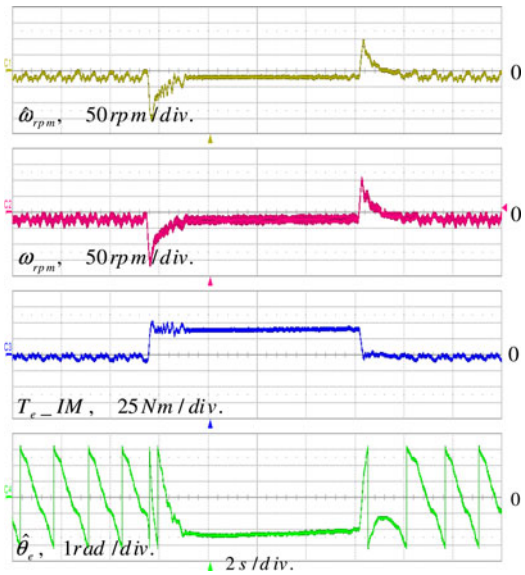

Fig. 13. Experimental results at zero synchronous frequency (44 N·m was applied at the constant speed of –20 r/min.).

the zero frequency operation, the torque and speed were under control. Fig. 14 shows similar waveforms with load torques of 40 and 50 N·m. For simplicity, $\hat{\omega}_{\rm rpm}$ and $\omega_{\rm rpm}$ are omitted. Under no-load conditions, $\hat{\theta}_e$ is the same in all three figures. When loads were applied, the frequencies of $\hat{\theta}_e$ differed slightly due to their slip frequencies. The respective frequencies of $\hat{\theta}_e$ were 0, –0.07, and 0.1 Hz.

Based on the experimental results shown in these figures, it can be concluded that the proposed method is robust with respect to overall loading conditions, and provides reasonable performance at low frequencies, including zero.

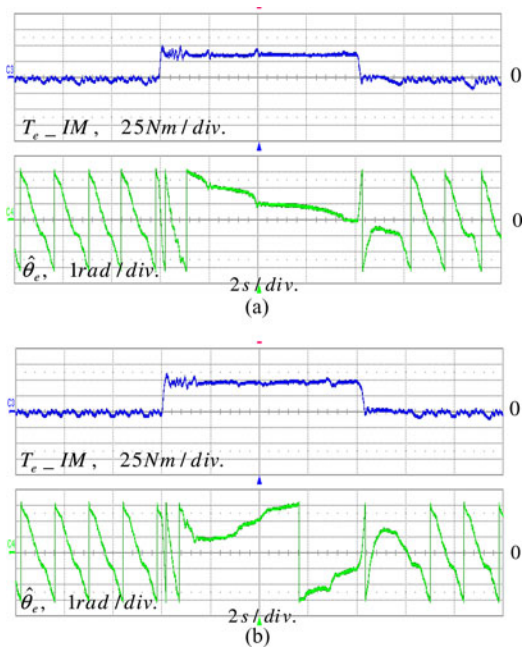

Fig. 14. Experimental results near zero synchronous frequency: (a) 40 N·m and (b) 50 N·m were applied at the constant speed of –20 r/min.

V. Conclusion

This paper proposed a sensorless control method for induction machines, using a square-wave voltage injection into the q-axis. This study considered two nonideal phenomena that severely degrade the performance of sensorless controls for induction machines. Multiple saliency problems can be overcome by injecting a square-wave signal into the estimated synchronous reference frame. By injecting the square-wave signal into the q-axis, the robustness of rotor flux position estimation with respect to load conditions and operating speed can be enhanced. Variation of saliency characteristics can easily be compensated by a linear function of the torque command. The experimental results showed reasonable performances, even when the reference speed changed slowly near zero speed and when load torque disturbances occurred at low frequencies, including zero stator frequency.

References

[1] B. Metidji, N. Taib, L. Baghli, T. Rekioua, and S. Bacha, "Low-cost direct torque control algorithm for induction motor without ac phase current sensors," *IEEE Trans. Power Electron.*, vol. 27, no. 9, pp. 4132–4139, Sep. 2012.

[2] Y. Liu, J. Zhao, R. Wang, and C. Huang, "Performance improvement of induction motor current controllers in field-weakening region for electric vehicles," *IEEE Trans. Power Electron.*, vol. 28, no. 5, pp. 2468–2482, May 2013.

[3] P. Vas, *Sensorless Vector and Direct Torque Control.* New York, NY, USA: Oxford Univ. Press, 1998, pp. 122–124.

[4] M. Tursini, R. Petrella, and F. Prasiliti, "Sensorless control of an IPM synchronous motor for city-scooter application," in *Proc. Conf. Rec. IEEE IAS. Annu. Meeting*, Oct. 2003, pp. 1472–1479.

[5] K. Ide, M. Takaki, S. Morimoto, Y. Kawazoe, A. Maemura, and M. Ohto, "Saliency-based sensorless drive of adequate designed IPM motor for robot vehicle application," in *Proc. Conf. Rec. PCC*, Apr. 2007, pp. 1126–1133.

[6] H. Choi, N. T. Vu, and J. W. Jung, "Digital implementation of an adaptive speed regulator for a PMSM," *IEEE Trans. Power Electron.*, vol. 26, no. 1, pp. 3–8, Jan. 2011.
[7] S. Ogasawara and H. Akagi, "An approach to position sensorless drive for brushless dc motor," *IEEE Trans. Ind. Appl.*, vol. 27, pp. 928–933, Sep./Oct. 1991.
[8] S. Ogasawara and H. Akagi, "Implementation and position control performance of a position-sensorless IPM motor drive system based on magnetic saliency," *IEEE Trans. Ind. Appl.*, vol. 34, no. 4, pp. 806–812, Jul./Aug. 1998.
[9] M. A. Vogelsberger, S. Grubic, T. G. Habelter, and T. M. Wolbank, "Using PWM-induced transient excitation and advanced signal processing for zero-speed sensorless control of AC machines," *IEEE Trans. Ind. Electron.*, vol. 57, no. 1, pp. 365–374, Jan. 2010.
[10] S. I. Yong, J. W. Choi, and S. K. Sul, "Sensorless vector control of induction machine using high frequency current injection," in *Proc. Conf. Rec. IEEE-IAS Annu. Meeting*, 1994, pp. 503–508.
[11] P. L. Jansen and R. D. Lorenz, "Transducerless position and velocity estimation in induction and salient AC machines," *IEEE Trans. Ind. Appl.*, vol. 31, no. 2, pp. 240–247, Mar./Apr. 1995.
[12] F. Briz and M. W. Degner, "Rotor position estimation," *IEEE Ind. Electron. Mag.*, no. 2, pp. 24–36, Jun. 2011.
[13] J. I. Ha and S. K. Sul, "Sensorless field-orientation control of an induction machine by high-frequency signal injection," in *Proc. Conf. Rec IEEE-IAS Annu. Meeting*, 1997, pp. 426–432.
[14] M. J. Corley and R. D. Lorenz, "Rotor position and velocity estimation for a permanent magnet synchronous machine at standstill and high speeds," in *Proc. Conf. Rec. IEEE-IAS Annu. Meeting*, 1996, vol. 1, pp. 36–41.
[15] J. H. Jang, S. K. Sul, J. I. Ha, K. Ide, and M. Sawamura, "Sensorless drive of surface-mounted permanent-magnet motor by high-frequency signal injection based on magnetic saliency," *IEEE Trans. Ind. Appl.*, vol. 39, no. 4, pp. 1031–1039, Jul./Aug., 2003.
[16] Y. D. Yoon, S. K. Sul, S. Morimoto, and K. Ide, "High bandwidth sensorless algorithm for AC machines based on square-wave type voltage injection," *IEEE Trans. Ind. Appl.*, vol. 47, no. 3, pp. 1361–1370, May/Jun. 2011.
[17] R. Leidhold and P. Mutschler, "Improved method for higher dynamics in sensorless position detection," in *Proc. Conf. Rec. IECON*, Nov. 10–13, 2008, pp. 1240–1245.
[18] S. Kim, J. I. Ha, and S. K. Sul, "PWM switching frequency signal injection sensorless method in IPMSM," *IEEE Trans. Ind. Appl.*, vol. 48, no. 5, pp. 1576–1587, Sep./Oct. 2012.
[19] D. Basic, F. Malrait, and P. Rouchon, "Current controller for low-frequency signal injection and rotor flux position tracking at low speeds," *IEEE Trans. Ind. Electron.*, vol. 58, no. 9, pp. 4010–4022, Sep. 2011.
[20] V. M. Leppanen and J. Luomi, "Observer using low-frequency injection for sensorless induction motor control—Parameter sensitivity analysis," *IEEE Trans. Ind. Electron.*, vol. 53, no. 1, pp. 216–224, Feb. 2006.
[21] M. W. Degner and R. D. Lorenz, "Using multiple saliencies for the estimation of flux, position, and velocity in AC machines," *IEEE Trans. Ind. Appl.*, vol. 34, no. 5, pp. 1097–1104, Sep./Oct. 1998.
[22] C. Caruana, G. M. Asher, and M. Sumner, "Performance of HF signal injection techniques for zero-low-frequency vector control of induction machines under sensorless conditions," *IEEE Trans. Ind. Electron.*, vol. 53, no. 1, pp. 225–238, Feb. 2006.
[23] P. L. Jansen and R. D. Lorenz, "Transducerless field orientation concepts employing saturation-induced saliencies in induction machines," *IEEE Trans. Ind. Appl.*, vol. 32, no. 6, pp. 1380–1393, Nov./Dec. 1996.
[24] T. Wolbank, J. Machl, R. Wohrnschimmel, and H. Hauser, "Interaction of induction machines fundamental wave design and asymmetries in the transient electrical behavior caused by saturation," in *Proc. Conf. Rec. IEEE IECON'03*, Roanoke, VA, USA, 2003, pp. 1453–1459.
[25] H. Kubota, K. Matsuse, and T. Nakano, "DSP-based adaptive flux observer of induction motor," *IEEE Trans. Ind. Appl.*, vol. 29, no. 2, pp. 344–348, Mar./Apr. 1993.

Young-Doo Yoon (S'06–M'10) was born in Korea. He received the B.S., M.S., and Ph.D. degrees in electrical engineering from Seoul National University, Seoul, Korea, in 2002, 2005, and 2010, respectively.

From 2010 to 2013, he was with SAMSUNG Electronics Company, Korea, as a Senior Engineer. Since 2013, he has been an Assistant Professor in the Department of Electrical Engineering, Myongji University, Yongin, Korea. His current research interests include power-electronic control of electric machines, high power converter, and electric home appliances.

Seung-Ki Sul (S'78–M'80–SM'98–F'00) was born in Korea in 1958. He received the B.S., M.S., and Ph.D. degrees in electrical engineering from Seoul National University, Seoul, Korea, in 1980, 1983, and 1986, respectively.

From 1986 to 1988, he was an Associate Researcher with the Department of Electrical and Computer Engineering, University of Wisconsin, Madison, USA. From 1988 to 1990, he was a Principal Research Engineer with Gold-Star Industrial Systems Company. Since 1991, he has been a member of the Faculty of the School of Electrical Engineering, Seoul National University, where he is currently a Professor. His current research interests are power-electronic control of electric machines, electric/hybrid vehicle drives, and power-converter circuits.